Surface characteristics and permeability enhancement of shale fractures due to water and supercritical carbon dioxide fracturing

Yunzhong Jia [a,b,*], Yiyu Lu [a], Derek Elsworth [b], Yi Fang [c], Jiren Tang [a]

[a] State Key Laboratory for Coal Mine Disaster Dynamics and Control, Chongqing University, Chongqing, 400044, China
[b] Department of Energy and Mineral Engineering, EMS Energy Institute, and G3 Center, The Pennsylvania State University, University Park, PA 16802, United States
[c] Institute for Geophysics, Jackson School of Geosciences, The University of Texas at Austin, Austin, TX, 787122, United States

ARTICLE INFO

ABSTRACT

Carbon dioxide (CO$_2$) is an alternative working fluid to water for hydraulic fracturing in shale reservoirs. It offers advantages as a substitute for the use of large quantities of potable water and for the concurrent sequestration of CO$_2$, however sorption and swelling effects, and their impact on permeability may be detrimental and are undefined. Hence, it is of great importance to understand the mechanism of supercritical carbon dioxide fracturing in shale and its effect on shale permeability enhancement. We conduct hydraulic fracturing experiments on shale samples using both water (H$_2$O) and supercritical carbon dioxide (Sc-CO$_2$) as fracturing fluids to explore the surface characteristics and permeability evolution of fluid-driven fractures. We use profilometry to measure the roughness and complexity of the resulting fracture surfaces and measure the permeability of the fractures. Results indicate that: (1) Sc-CO$_2$ fracturing creates fractures with larger tortuosity relative to H$_2$O fracturing (macroscale); (2) the topography of Sc-CO$_2$ fracture surfaces is more rough and complex compared to that of H$_2$O fractured surfaces; (3) larger mineral grains are removed and relocated from induced fracture surfaces by Sc-CO$_2$ fracturing – these acting as micro proppants that result in a larger fracture aperture; (4) correspondingly, the permeability of shale fractures increases by ~5 orders of magnitude with Sc-CO$_2$ fracturing and this enhancement is ~3 orders of magnitude higher than that by traditional hydraulic fracturing. This observation potentially validates the feasibility of Sc-CO$_2$ as a fracturing fluid for the stimulation of shale reservoirs.

1. Introduction

Over the last decade, shale gas has been successfully recovered in the United States due to the application of improved techniques of horizontal drilling and massive hydraulic fracturing (Arthur et al., 2008; Miller et al., 2011; Palmer et al., 2007; Yuan et al., 2017, 2015b). Hydraulic fracturing, as the most critical process of this ensemble of techniques, is implemented by injecting a large volume of water-based fluid to create wing-shaped tensile fractures that propagate away from the wellbore and connect to pre-existing natural fractures in the shale reservoir (McClure, 2014). The fracturing fluid is the most vital component of this technology, could significantly affect the enhancement of permeability by creating fractures which are main flow channels for fracturing fluid, hydrocarbon and other fluids (Odumabo et al., 2014). Now, water-based fracturing fluid is most commonly used whose rheology and non-Newtonian fluid flow in porous media has been investigated carefully (Ciriello et al., 2016; Federico et al., 2017; Longo et al., 2015). In

addition, efforts have been made to develop various models to predicate shale recovery efficiency and optimize well fracture which include: multi-linear flow solution to characterize the effects of non-uniform fracture intensities on well production (Yuan et al., 2015a), apply an intergated production history evaluation workflow to optimize well spacing (Clarkson, 2013; Yuan et al., 2017), and propose a novel concept of dynamic-drainage-volume (DDV) method to describe long-term transient flow in shale (Yuan et al., 2016). However, there are some drawbacks to water-based fracturing fluid. For instance, water may alter the mechanical properties of clay-rich shale reservoir formations, react with clay minerals and close fractures which created by fracturing operations and reduce the stimulation efficiency (Lu et al., 2016; Jia et al., 2017). Moreover, environmental issues, such as the shortage of surface water for hydraulic fracturing in arid areas (Scanlon et al., 2014; Vengosh et al., 2014), potential groundwater contamination caused by additives in fracturing fluid (Myers, 2012; Osborn et al., 2011; Vengosh et al., 2013), and induced seismicity by large-scale wastewater disposal and flow-back

---

water re-injection (Fang et al., 2017; Shapiro and Dinske, 2009; C. C. Wang et al., 2017; Warpinski et al., 2012) have raised public concerns. To avoid those drawbacks, supercritical carbon dioxide (Sc-CO_2) has been proposed as an alternative fracturing fluid for hydraulic fracturing operations (Ishida et al., 2012; Middleton et al., 2015; Pei et al., 2015).

Previous investigations of Sc-CO_2 fracturing concluded that there were some advantages which included greater fracture propagation (Ishida et al., 2012; Li et al., 2016), reducing flow blockages and desorption (Middleton et al., 2015) and the potential for concurrent CO_2 sequestration (Dahaghi, 2010). Former fracturing tests in granite indicates that Sc-CO_2 fracturing results in a smaller breakdown pressure under low confining stress compared with water (Ishida et al., 2012, 2016). Fracturing experiments in Green River shale and Longmaxi shale also demonstrate that Sc-CO_2 fracturing produces a more extensive and interconnected fracture network than water based on profilometry and CT scanning methods (Li et al., 2016; Zhang et al., 2016). Simulation works also verified that Sc-CO_2 fracturing has a lower breakdown pressure and develop fractures with greater complexity (J. Wang et al., 2017). Calculation of temperature in fracture during Sc-CO_2 fracturing verified the CO_2 phase transition during whole fracturing process (J. S. Wang et al., 2016a,b). Positron emission tomography (PET) has been used to explicitly visualize CO_2 flow in shale during injection experiments; the enhanced oil recovery factor could reach as high as 55% without fracturing the sample (Fernø et al., 2015). However, the topography of fracturing induced surfaces and the enhancement of permeability remain poorly explained for Sc-CO_2 fracturing. In addition, few comprehensive experiments have verified the feasibility of Sc-CO_2 fracturing in shale to increase the permeability and thereby promote gas transport by the creation of effective fractures or in the improved connection of natural fractures.

In this study, Sc-CO_2 and H_2O are used as the fracturing fluids in Longmaxi shale – a principal shale gas producer in the Sichuan basin, China. After fracturing, the surface profile of the fracture is scanned by stylus and optical profilometry to quantify roughness and complexity. In addition, we measure the permeability of the fractures both before and after fracturing with both H_2O and Sc-CO_2. The relationship between fluid characteristics and induced fracture surface characteristics is constrained to better understand mechanisms of Sc-CO_2 fracturing.

2. Experimental methods

This experimental study comprises three interrelated components: first, we conduct hydraulic fracturing experiments with both H_2O and Sc-CO_2 under the same controlling conditions; then we perform micro-characterization of fracture surfaces to define how these two fluids influence the resulting surface topography of the generated fractures; finally, we measure the permeability of the newly fractured shale cores to examine the effects of H_2O and Sc-CO_2 on the enhancement of fracture permeability.

2.1. Sample material and preparation

The shale samples are collected from the Lower Silurian Longmaxi Formation, which is the most successful shale gas production area in the Sichuan basin (northwest of Chongqing, China). The black shale is fine-grained, highly laminated and with low-grade kerogen (Lu et al., 2016). Natural fractures are not observable in the intact shale. The petrophysical properties and mineral compositions of the samples are listed in Table 1 and Table 2.

The samples are shown in Fig. 1. Research indicates that the propagation of the pressure waves is distorted in finite-size sample while relative steady in real deposit. However, in this experiment, attention is paid mainly on surface characteristics and fracture permeability, which means we could ignore the fluid pressure wave propagation in small samples (Longo and Di Federico, 2015). In order to eliminate the effect of moisture added during the coring process, the samples are oven dried for

Table 1
Petrophysical properties of the Longmaxi shale.

Parameters	Values	Units
Tensile Strength	13.5	MPa
Compressive Strength	136.0	MPa
Young's Modulus	25.0	GPa
Porosity	3.91%	–
Bulk Modulus	16.70	GPa
Poisson's ratio	0.25	–
TOC	0.55–4.41%	–

Table 2
Mineral compositions of the Longmaxi shale.

Minerals	Percentage (%)
Quartz	53.50
Calcite	20.30
Illite	9.80
Dolomite	8.70
Pyrite	3.60
Plagioclase	3.10
K-feldspar	1.00
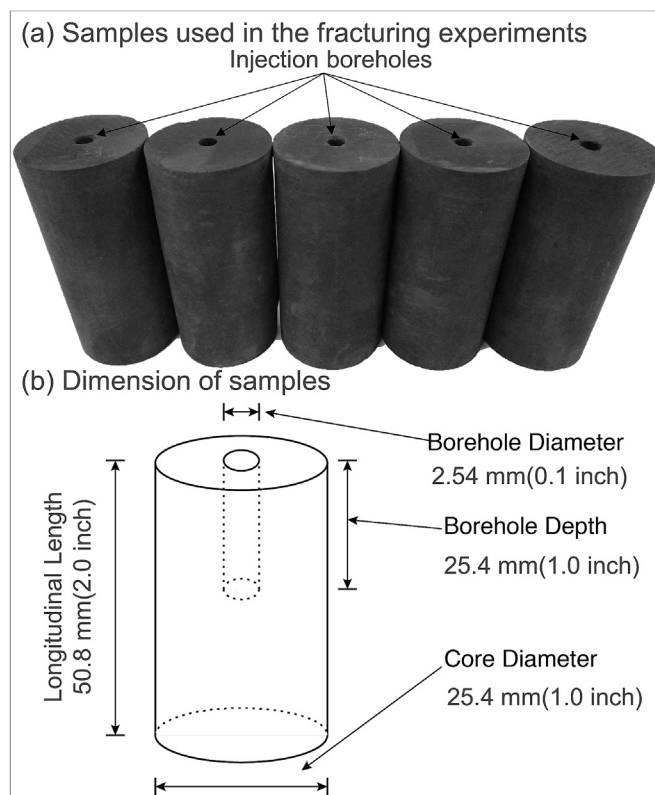
Fig. 1. (a) Samples used in the fracturing experiments; (b) The samples are cored to 25.4 mm (1-inch) in diameter and 50.8 mm (2-inch) in length; A blind central borehole (2.54 mm) is predrilled to a depth of 25.4 mm (1 inch) along the axis of the core as an analogue to an injection well.

24 h at 40 °C. Then the samples are used for the H_2O and Sc-CO_2 fracturing experiments.

2.2. Hydraulic fracturing experiments

The hydraulic fracturing experiments are performed with a triaxial testing apparatus that can independently apply confining stress, axial stress and perform fluid injection for fracturing (Fig. 2). The core samples
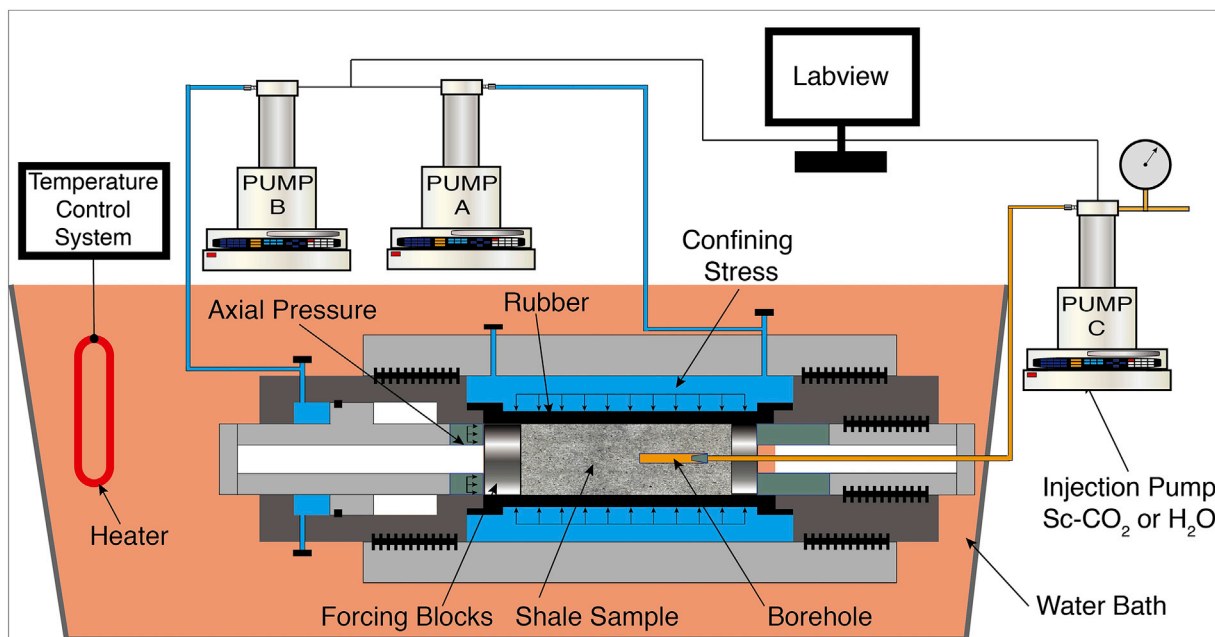
Fig. 2. Triaxial apparatus for fracturing: pump A controls the confining stress; pump B controls axial stress; pump C injects fracturing fluid (Sc-CO$_2$ or distilled water) at a constant flow rate of 3 mL/min. The prepared sample is placed between two stainless steel forcing blocks sealed with a rubber O-ring. The Temco cell is immersed in a water bath with temperature controlled by a heater (45 °C). The Temco cell is temperature-equilibrated within the water bath for 12 h before each fracturing tests.

are encased within a rubber jacket and installed within the triaxial core holder (Temco Cell). We first flow the fracturing fluid (Sc-CO$_2$ or distilled water) to saturate the sample assembly and fluid lines. Then, a confining stress of 10 MPa and axial stress of 15 MPa are applied gradually by syringe (ISCO) pump. After the applied stresses have reached steady state, the fracturing fluid is injected at a constant flow rate of 3 mL/min. When the injection pressure reaches the breakdown pressure of the sample, injection is ceased. For each type of fracturing fluid, we perform

experiments on six samples. Post-hydraulic fracturing, three of the fractured samples are used for fracture surface micro-characterization profilometry and the other three are used for permeability tests.

2.3. Micro-characterization of fracture surface

Post-hydraulic fracturing, the fractured samples with freshly exposed surfaces are scanned by profilometer to determine the fracture surface
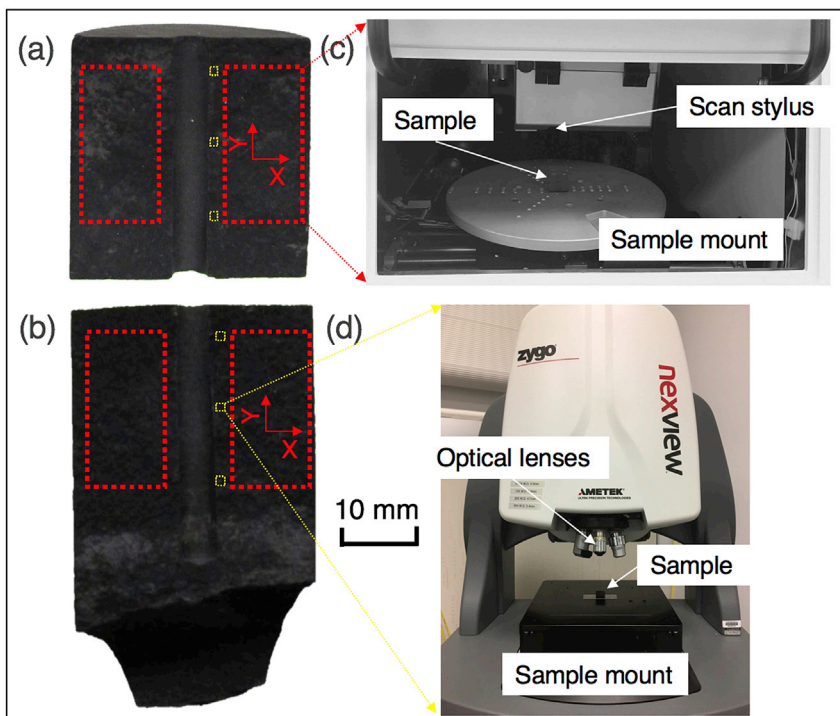
Fig. 3. (a) A sample fractured by H$_2$O; (b) A sample fractured by Sc-CO$_2$; (c) The dimension of the red sampling window is 20 mm × 10 mm for a stylus profilometry scan; (d) yellow sampling windows are used for optical profilometry near the injection borehole (dimension is 838.97 μm × 838.97 μm). (For interpretation of the references to colour in this figure legend, the reader is referred to the Web version of this article.)

roughness and complexity. Two types of profilometry measurements are made - stylus profilometry and optical profilometry, respectively. Stylus profilometry (model: KLA Tencor P16+) is a contact apparatus to determine fracture surface topography at a large scale. Two 20 mm × 10 mm windows on each exposed fracture surface are scanned as shown in Fig. 3. Three windows adjacent to the borehole are characterized at micro-scale (*i.e.*, 838.97 μm × 838.97 μm) with optical profilometry (model: Zygo Newview 3D). We then perform statistical analysis to capture the surface characteristics of fractures and to distinguish the effects between two fracturing fluids (*i.e.*, H_2O vs. Sc-CO_2).

Roughness and complexity are two crucial properties to describe fracture surface topography (Arakawa and Takahashi, 1991; Leach, 2013). These two properties of fracture surfaces are quantified by following parameters:

(1) The arithmetic mean (S_a) of the absolute value of the height within a sampling area expressed as (Gadelmawla et al., 2002):

$$S_a = \frac{1}{A} \int |z(x,y)| dxdy \tag{1}$$

(2) The root mean square (RMS) (S_q) of the surface departure within the sampling area defined as:

$$S_q = \frac{1}{A^2} \int |z^2(x,y)| dxdy \tag{2}$$

(3) The maximum height of the surface (S_z), defined as the absolute sum of the largest peak and largest valley depth elevations within the sampling area.
(4) The fractal dimension, *D*, is a ratio providing a statistical index of fracture complexity for comparing detailed pattern changes (Mandelbrot and Pignoni, 1983). A box-counting method is used to calculate the Minkowski fractal dimension *D*, which is expressed as (Pentland, 1984):

$$D = \lim_{N \to 0} \frac{\log M_N}{\log(1/N)} \tag{3}$$

where M_N is the minimum assembly number needed to cover target object in *N* diametric assembly. For a fracture surface, $2 < D < 3$ and a larger *D* value means a relatively complex surface while a smaller *D* describes a surface with less complexity.

2.4. Hydraulic conductivity measurement

Helium permeability is measured by the pulse decay method (Wang et al., 2015) to define permeability enhancement from fracturing. The use of helium gas avoids the potential effects of adsorption and/or associated swelling and change in permeability (Wang et al., 2015). These measurements are performed both before and after the fracturing using the experimental configuration of Fig. 4 (a). In the case where the samples do not fracture thorough out, we cut the intact part of the core from where the fracture propagation ends. In this way, the measured permeability is solely the fracture permeability with the matrix permeability of shale not affecting the experimental results.

The applied confining stress and axial stress are equal to that in the fracturing experiment. For a comparison, the matrix permeability was measured using three intact samples 5.08 mm (0.2-inch) long and 25.40 mm (1-inch) in diameter as shown in Fig. 4 (b).

Permeability is recovered from the pressure response as (Brace et al., 1968),
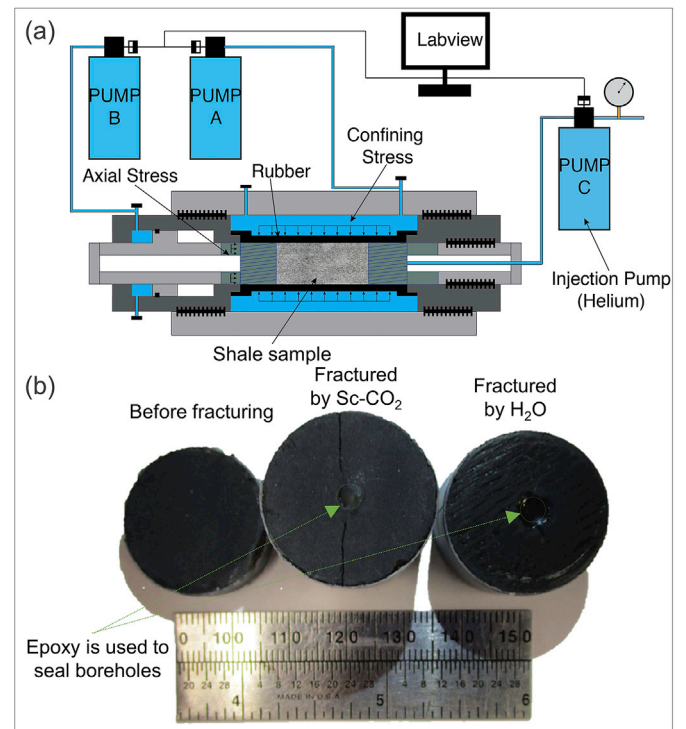
Fig. 4. (a) Apparatus for permeability measurement. Pump A controls the confining stress (10 MPa); pump B controls axial stress (15 MPa); pump C controls pore pressure; (b) Samples used in permeability measurements: before fracturing (left), fractured by Sc-CO_2 (middle), fractured by H_2O (right). The borehole drilled for the hydraulic fracturing test is sealed by epoxy to avoid its effect on permeability measurements. All tests are performed at room temperature (25 °C).

$$P_{up}^t - P_{down}^t = \left(P_{up}^{t_0} - P_{down}^{t_0} \right) \cdot e^{-\alpha t} \tag{4}$$

$$\alpha = \frac{kA}{\mu \beta L} \left(\frac{1}{V_{up}} + \frac{1}{V_{down}} \right) \tag{5}$$

where P_{up}^t [Pa] and P_{down}^t [Pa] are upstream and downstream pressures at time *t*; $P_{up}^{t_0}$ [Pa] and $P_{down}^{t_0}$ [Pa] are initial upstream and downstream pressures; the coefficient α[dimensionless] is recovered from the pressure decay curve; μ[Pa·s] is the dynamic viscosity of helium; β[Pa^{-1}] is the fluid compressibility; *L* [m] is the length of the sample; *A* [m^2] is the cross-sectional area of sample; V_{up} [m^3] and V_{down}[m^3] are volumes of the upstream and downstream reservoirs. Combining Eq. (4) and Eq. (5), the permeability *k* [m^2] is expressed as:

$$k = \frac{\mu \beta L}{A} \cdot \frac{V_{up} \cdot V_{down}}{V_{up} + V_{down}} \tag{6}$$

3. Experimental results

In this section, we first describe the macroscopic observations of the fracture and calculate the fracture tortuosity. We then interpret the measurements of the topographic properties of fracture surfaces by stylus and optical profilometry. Finally, the permeability data are analyzed to compare the permeability enhancement by Sc-CO_2 versus that by H_2O fracturing.

3.1. Fracture topography

For H_2O fracturing, the fracture partially transects the sample (Fig. 5) and for Sc-CO_2 fracturing the sample is fully transected into two halves.
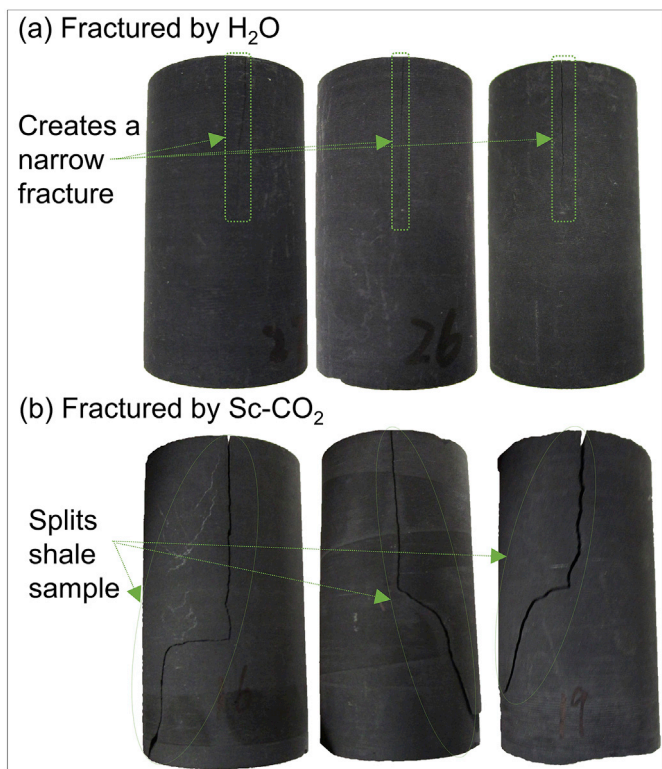
Fig. 5. Samples after fracturing. (a) Representative samples fractured by H_2O; (b) Representative samples fractured by Sc-CO_2. Sc-CO_2 fracturing splits the shale sample and conventional hydraulic fracturing creates a narrow fracture.

These results suggest that Sc-CO_2 is more energetic in developing fractures.

A tortuosity parameter is introduced to describe macro-observation of fracture topography as follows (Chen et al., 2015; Ishida et al., 2016):

$$C = \frac{L}{L_0} \tag{7}$$

C [dimensionless] is fracture tortuosity, L [m] is the total fracture length of a flow pathway; L_0 [m] is the linear length between the two ends of the fracture pathway.

Photographs of the fractured samples are digitized (Fig. 6) to determine the length of the fracture propagation pathway (black lines) and the linear length (red dashed lines). The calculated fracture tortuosity is shown in Fig. 7. Compared with data from Chen et al. whose research on
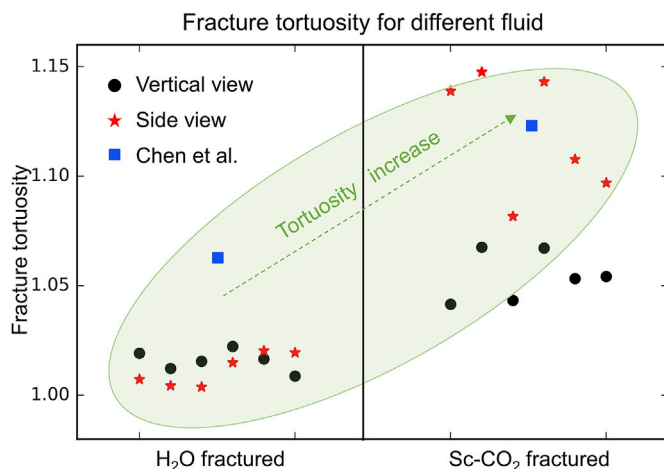
Fig. 7. Fracture tortuosity for different fluid induced fractures. Black circles recovered from the vertical view of the induced fractures and the red stars the side view. Blue squares recover from other scholar's data (Chen et al., 2015). (For interpretation of the references to colour in this figure legend, the reader is referred to the Web version of this article.)
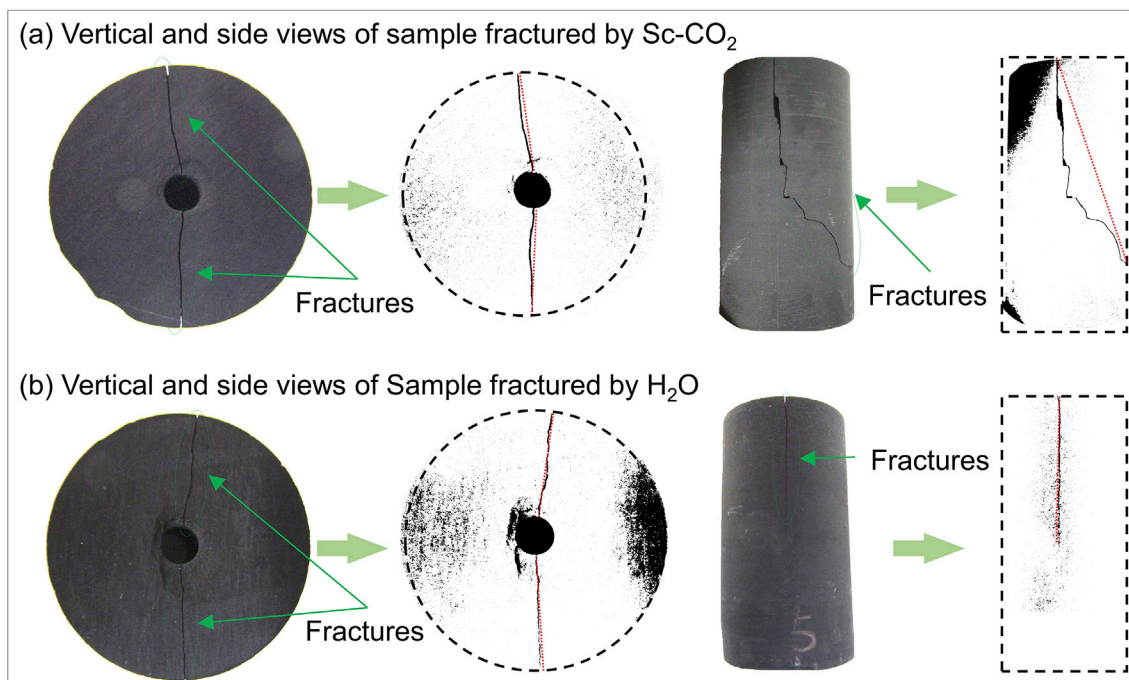
Fig. 6. Schematic of fracture tortuosity calculation: (a) vertical and side views of sample fractured by Sc-CO_2; (b) vertical and side views of sample fractured by H_2O.
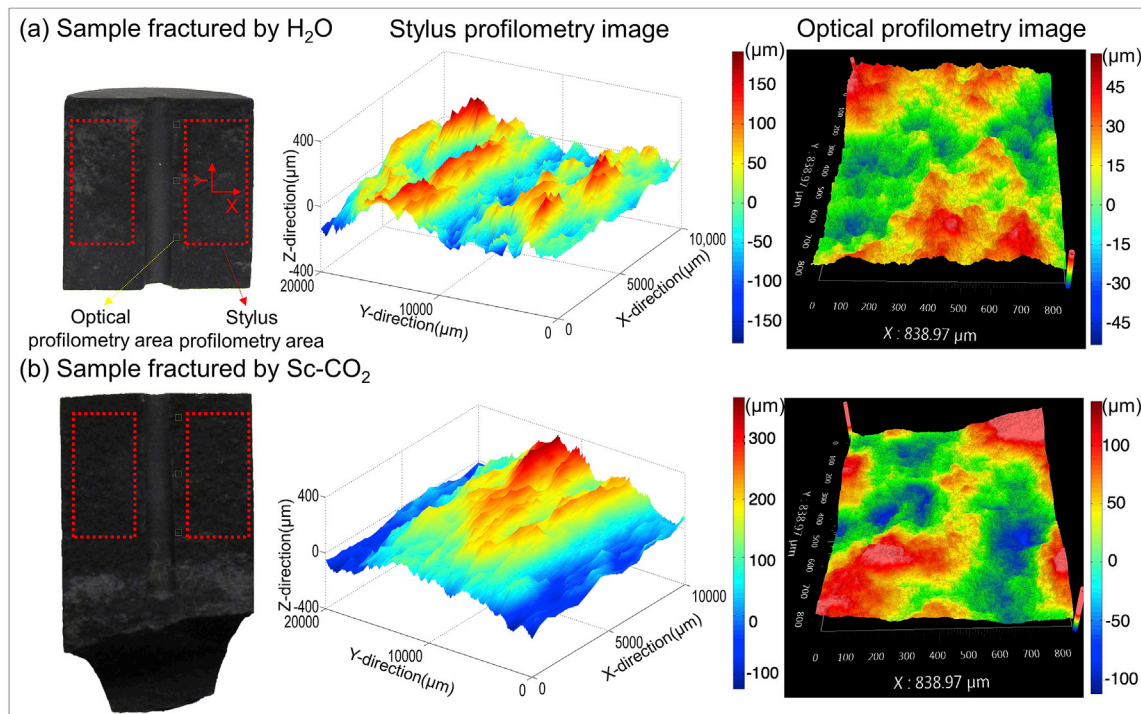
Fig. 8. Profilometry images for Sc-CO$_2$ and H$_2$O fracturing. (a) Sample fractured by H$_2$O; (b) Sample fractured by Sc-CO$_2$. The red observation windows are scanned in the stylus profilometry measurements and the yellow windows in the optical profilometry. (For interpretation of the references to colour in this figure legend, the reader is referred to the Web version of this article.)

sandstone with different fluid fracturing, Sc-CO$_2$ fracturing creates a higher fracture tortuosity (ranges from 1.0415 to 1.1832) than that of H$_2$O (ranges from 1.0038 to 1.0223), suggesting that Sc-CO$_2$ is more effective in developing tortuous fractures.

3.2. Fracture surface characterization

Representative images from the stylus and optical profilometry are shown in Fig. 8. The surface characteristics induced by Sc-CO$_2$ and H$_2$O are discussed in sections 3.2.1 and 3.2.2.

3.2.1. Stylus profilometry results

The topographic characteristics (S_a, S_q, S_z and fractal dimension D) recovered from the stylus profilometry are shown in Fig. 9. Sc-CO$_2$ fractured fractures have a larger mean value of S_a, S_q and S_z, suggesting rougher surfaces induced by Sc-CO$_2$. From the standpoint of complexity, the fractal dimension of the Sc-CO$_2$ fractured surface ranges from 2.2314 to 2.2660, larger than that of the H$_2$O fractured surface (ranges from 2.0855 to 2.1058), suggesting that Sc-CO$_2$ fracturing creates more *complex* fracture surfaces than H$_2$O fracturing.

3.2.2. Optical profilometry results

The optical profilometry results which includes topographic characteristics (S_a, S_q, S_z and fractal dimension D) are shown in Fig. 10. At micro scale, similar results and conclusions can be derived for optical profilometry tests near the injection wellbore. Optical profilometry shows that Sc-CO$_2$ fractured surfaces have a higher mean (S_a) and RMS (S_q) values which illustrate rougher fracture surfaces. Sc-CO$_2$ fracturing also creates a surface with higher peaks and lower valleys near the injection wellbore, which contributes to a higher absolute height (S_z). These results are in accordance with stylus profilometry and consistent with the conclusion that the roughness parameters (S_a, S_q and S_z) have a positive relation with the scale of the sampled area (Candela et al., 2009; Renard et al., 2006). Sc-CO$_2$ fractured surfaces also show a larger fractal dimension D, representing a more complex fracture surface near the

injection borehole.

3.3. Permeability measurements

The permeability of each sample with increasing effective stress is shown in Fig. 11, indicating that the helium permeability of the matrix decreases with increasing effective stress. The matrix permeability of Longmaxi shale is of the order of $\sim 10^{-21}$ m^2 before fracturing. Sc-CO$_2$ fracturing increases the permeability by three orders of magnitude larger than that of fracturing with H$_2$O.

4. Discussion

We discuss potential mechanisms that may control the observed difference in fracture topography (roughness and complexity) due to fracturing with different fluids. Then, we explore the anticipated behavior for the flow of helium in a single fracture and constrain the relationship among fracture roughness, fracture permeability and fracture effective hydraulic aperture. Finally, we discuss potential primary causes for increased permeability enhancement when fracturing by Sc-CO$_2$ rather than by H$_2$O.

4.1. Impact of fluid characteristics on fracture surface topography

Two different mechanisms that vary in fracture initiation and fracture propagation determine fracture surface topography: (1) near the injection well, viscosity controls the invasion of fluid into the formation through diffusion before fracture initiation. This process is a time-dependent process; (2) Distal from the injection well, capillary effects and modes of fracture propagation control the fracture surface topography. As fracture propagation speed could up to 30 m/s (Renshaw and Harvey, 1994), this behavior is considered as time-independent.

4.1.1. Diffusion adjacent to the injection well pre-breakdown

Near the borehole, the low viscosity of the injected fluid results in a
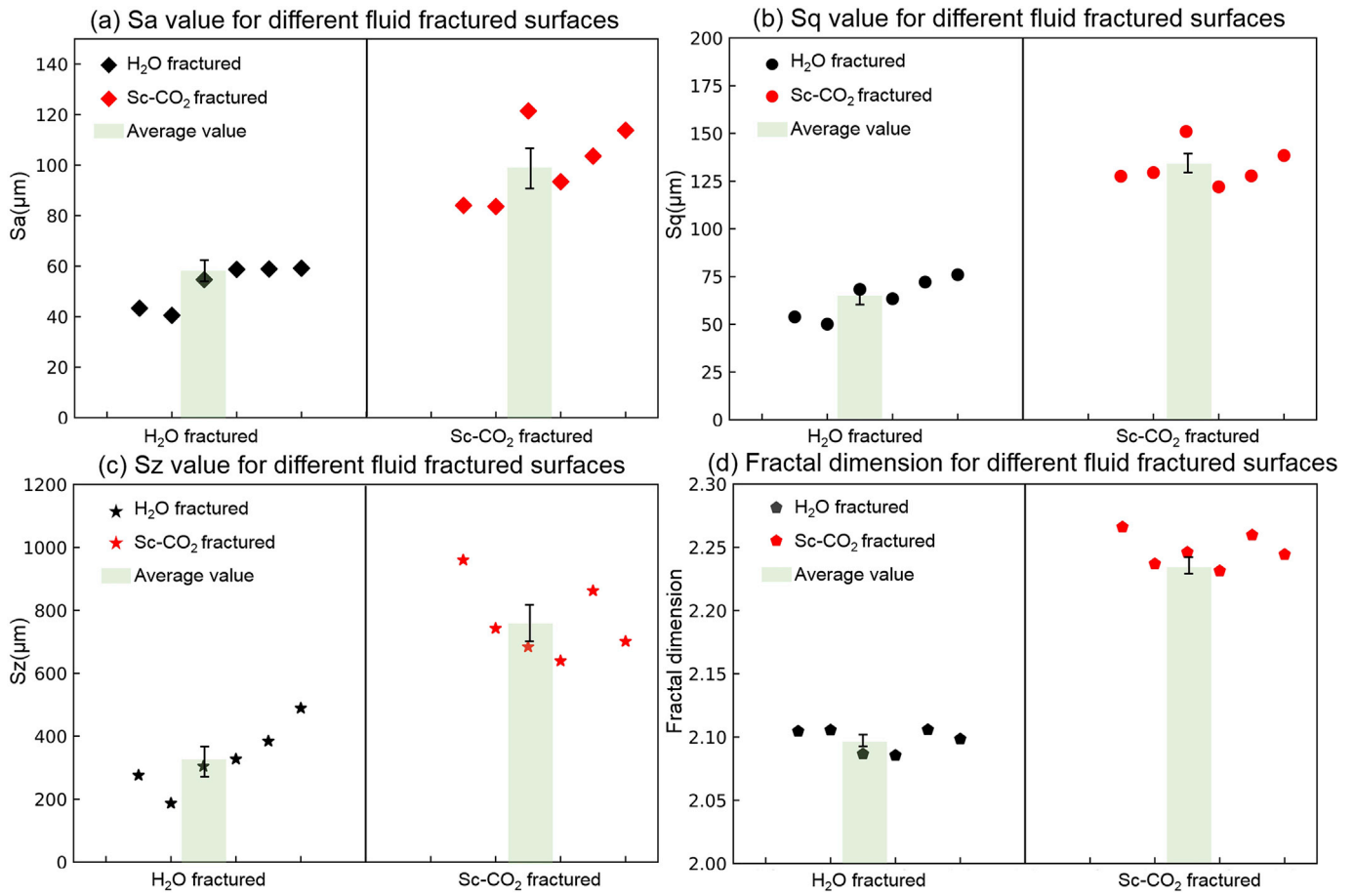
Fig. 9. Topographic parameters recovered for H_2O fractured surfaces and Sc-CO_2 fractured surfaces by stylus profilometry scan. (a) S_a; (b) S_q; (c) S_z; (d) fractal dimension D.

high diffusivity of Sc-CO_2, which is capable of inducing a rougher fracture surface. Fig. 12 shows the relationship among fluid pressure, viscosity and density for Sc-CO_2 and H_2O (Kestin et al., 1984; Fenghour et al., 1998). The viscosities of Sc-CO_2 and H_2O are ~108.28 μPa s and ~885 μPa s respectively at a pressure of 50 MPa and temperature of 45 °C. The resulting effective diffusion coefficient of Sc-CO_2 in shale is therefore ~2.2×10^{-8} m²/s (Fernø et al., 2015) and that for water estimated as ~4.44×10^{-9} m²/s based on kinetic theory. The diffusion length is defined as (Philibert, 2006):

$$x = \sqrt{4D_d \cdot t} \tag{8}$$

where x [m] is the diffusion length; D_d [m²/s] is diffusion coefficient; t [s] is diffusion time.

Based on pressure vs. time curve during fracturing tests which shown in Fig. 13, we use 100 s for H_2O fracturing and 150 s for Sc-CO_2 fracturing as diffusion time. The diffusion depth of Sc-CO_2 fracturing is 3633.18 μm while 1332.67 μm for H_2O fracturing. Hence, a larger penetration depth from the fracture may result for Sc-CO_2. For the breakdown process, shale breaks along the direction of the maximum principal stress as described by the maximum tensile stress criterion (Hossain et al., 2000; Hubbert and Willis, 1957). However, in reality, the hydraulic fracture will initiates from a weak point around the borehole (Detournay, 2016) as micro defects always will always be present (Fig. 14 (a)). During fluid injection, these defects may act as fluid channels where fracturing fluid can diffuse into the shale formation. For Sc-CO_2 fracturing, a larger diffusion coefficient would result in a larger diffusion length and area.

Comparing the diffusion depth with the optical profilometry measurements near the injection wellbore (Fig. 10(c)), fracture's roughness

parameter S_z induced by Sc-CO_2 fracturing are ~1.51 times larger than for H_2O fracturing (156.8749 μm vs. 104.2358 μm). This observation suggests a mechanism that fracturing fluid with smaller viscosity leads to a larger diffusion depth around the injection wellbore and the pre-existing micro-defects. When breakdown occurs, induced fractures created randomly in affected area and in areas where secondary fractures are widened, eventually leading to a larger fracture surface roughness and complexity.

4.1.2. Capillary effect on fluid invasion into pore throats

Stylus profilometry results indicate that Sc-CO_2 creates a rougher fracture surface in the distal area from the injection borehole. In the far field from the borehole (Fig. 14 (b)), capillary effects dominate fluid (Sc-CO_2 and H_2O) invasion into the shale matrix. In such a case, the pore structure serves as a significant influencing factor. Given a particular pore structure, the breakthrough/entry pressure (P_c^*) is determined by the pressure-independent interfacial tension (σ) and contact angle (θ). Thus, the pressure required for fluid to enter a pore throat is calculated as (Espinoza and Santamarina, 2010):

$$P_c^* = \frac{4\sigma \cos\theta}{d^*} \tag{9}$$

where P_c^* [Pa] is the entry pressure for fluid to enter the pore throat; σ [N/m] is interfacial tension; θ [°] is the contact angle; and d^* [m] is the critical pore throat size that fluid may enter.

In Eq. (9), the critical pore throat size is positively correlated with interfacial tension and the cosine of the contact angle. The interfacial tension of Sc-CO_2 is approximately constant at 20–30 mN/m at pressures
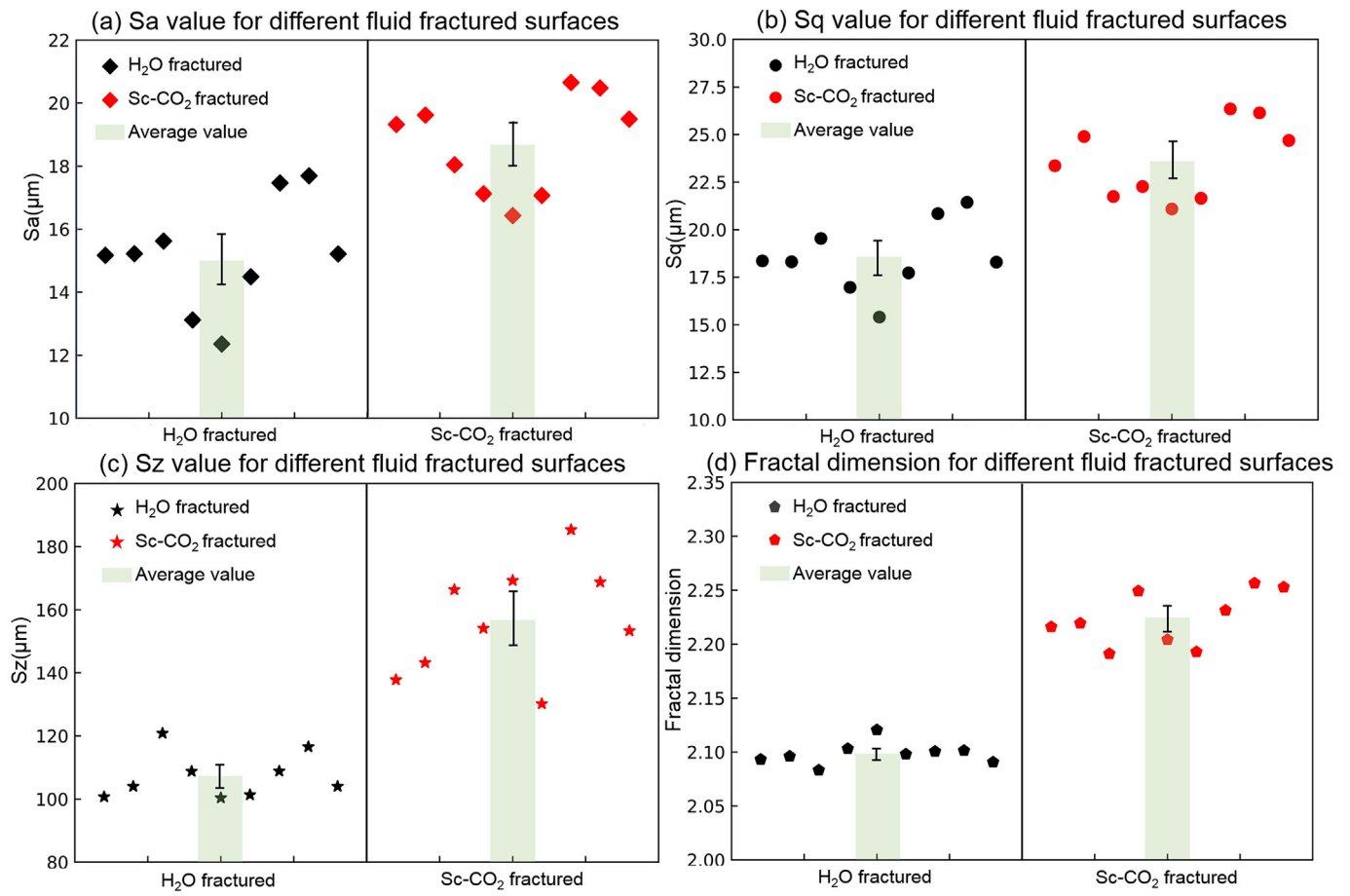
Fig. 10. Comparison of topographic parameters for H_2O fractured surfaces and Sc-CO_2 fractured surfaces recovered by optical profilometry. (a) S_a; (b) S_q; (c) S_z; (d) fractal dimension D.
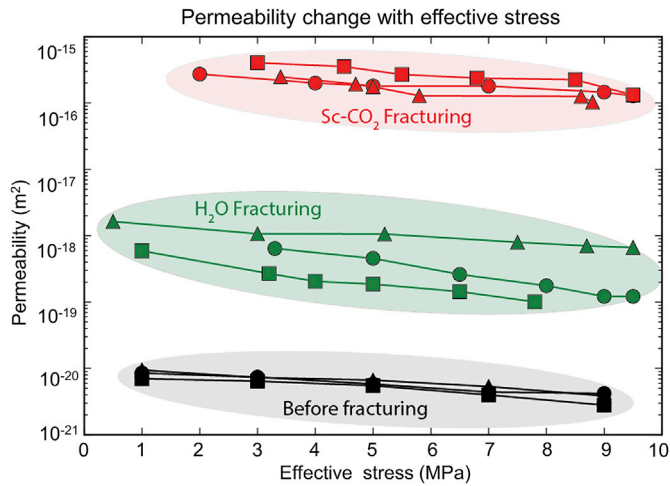
Fig. 11. Permeability change with effective stress for non-fractured and Sc-CO_2 and H_2O fractured samples. After Sc-CO_2 fracturing, the permeability increases to $\sim 10^{-16} \, m^2$, while after H_2O fracturing, the permeability only increases to $\sim 10^{-19} \, m^2$.

larger than $\sim 10 \, MPa$ while the interfacial tension of water is ~ 50–$70 \, mN/m$ (Espinoza and Santamarina, 2010; S. Z. Wang et al., 2016a,b). In shales, the contact angle of Sc-CO_2 is close to $0°$ while water has a contact angle of $\sim 15°$ (Espinoza and Santamarina, 2010). The breakthrough pressure in shale is $\sim 21 \, MPa$ (Espinoza and Santamarina, 2010). Thus, Sc-CO_2 may enter through shale pore throats as small as

5.7 nm (interfacial tension $\sim 30 \, mN/m$) while water is restricted to pore throats larger than 12.9 nm (interfacial tension $\sim 70 \, mN/m$). This suggests that under the same injection pressure, Sc-CO_2 could enter the pore throats whose diameter ranges between 5.7 nm and 12.9 nm while H_2O will be excluded. For this reason, Sc-CO_2 is more likely to enter smaller pore throats than H_2O in the far field from the injection well, which could result in larger volumes (scales with penetration volume) being invaded by Sc-CO_2, when breakdown occurs.

4.1.3. Fluid lag in fluid-drive fracture tip during fracture propagation

As another potential mechanism, we posit the fracture propagation type may affect the fracture surface roughness and complexity.

For a 2-D fracture tip, the fluid lag zone at the fluid-driven fracture tip is described as (Garagash and Detournay, 2000):

$$L_\mu = \frac{12\mu V E'}{\sigma_0^3} \tag{10}$$

$$L_\kappa = \frac{8}{\pi} \left(\frac{K_{IC}}{\sigma_0} \right)^2 \tag{11}$$

$$\kappa = \left(\frac{L_\kappa}{L_\mu} \right)^{\frac{1}{2}} \tag{12}$$

$$\lambda = \Lambda \cdot L_\mu \tag{13}$$

where L_μ [m] is a parameter associated with viscous dissipation (Desroches et al., 1994); μ [Pa·s] is fluid viscosity; V [m/s] is the fracture and fluid propagation velocity; E' [GPa] is the plane-strain modulus, which
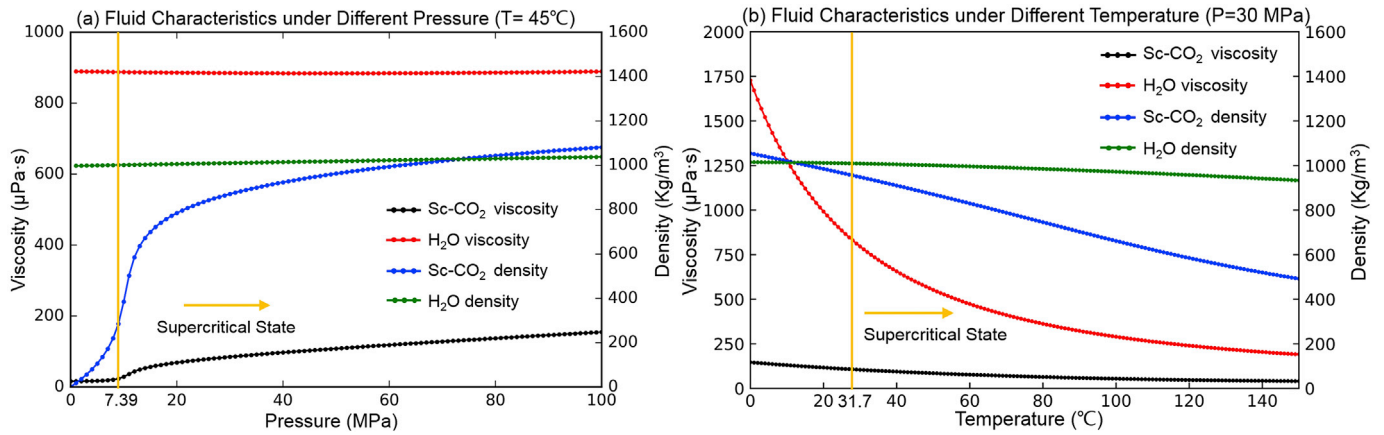
Fig. 12. (a). CO_2 and H_2O viscosity and density change with pressure at the temperature of 45 °C.At certain temperature, the viscosity and density of H_2O is approximately constant with pressure while the viscosity and density of CO_2 increase with pressure, especially as its turns supercritical; (b) CO_2 and H_2O viscosity and density change with temperature at constant pressure. At certain pressure, two fluid viscosity decrease when temperature increase.
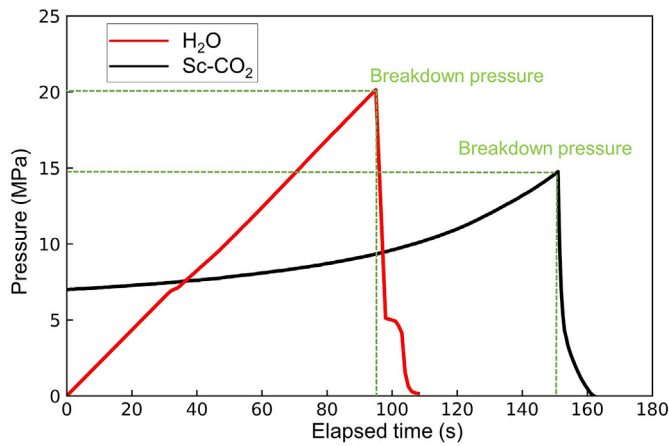
Fig. 13. Representative fracturing pressure versus time curves during fracturing tests. Due to the low compressibility of water, hydraulic fracturing elapsed time is smaller than that of Sc-CO_2 fracturing.

could be expressed as: $E' = E(1 - \nu^2)$, where E[GPa] is the Young's modulus and ν [dimensionless] is the Poisson ratio; σ_0[MPa] is far-field stress; K_{IC}[MPa·m$^{1/2}$] is the fracture toughness; L_κ[m] is a parameter that characterizes the dissipation due to fracturing of the solid; κ[dimensionless] is a dimensionless toughness; λ[m] is the fluid lag

length and Λ[dimensionless] is dimensionless fluid lag length.

In addition, numerical calculation method was deployed by Garagash which found that a larger dimensionless toughness κ leads to a smaller dimensionless lag length Λ and it is illustrated as in Fig. 15 (Garagash and Detournay, 2000).

Eq. (10)–(13) and Fig. 15 are used to estimate the fluid lag length in water-driven fracture and Sc-CO_2 driven fracture. The parameter used in estimation and the results are listed in Table 3.

The estimation results indicates that smaller viscosity Sc-CO_2 fluid creates fluid-driven fractures with a small fluid lag length $\sim 2.61996 \times 10^{-5}$ µm, while fluid lag length in water-driven fracture is 119.247 µm. In the fracture propagation process, low viscosity Sc-CO_2 is more easily reach the fracture tip, penetrating to the shale matrix, and leading to a more complex stress field at fracture tip. Conversely, when the fluid cannot reach the fracture tip, the far-field stress state controls the fracture propagation in a direction parallel to the maximum principal stress. This phenomenon has been commonly observed in H_2O fracturing experiments and also in our experiments (Detournay, 2004; Detournay and Carbonell, 1997; Ishida et al., 2012).

In summary, we posit an assumption that the direction of fracture propagation is not only controlled by far-field stress state, but also by fluid viscosity. At the macroscopic scale, the far-field stress state will make the fracture propagate parallel to the maximum principal stress direction. At microscopic scale, the penetration of a low viscosity fluid leads to a small fluid lag at the fracture tip, penetration into shale matrix and into smaller pore throats. This may create a fracture surface with
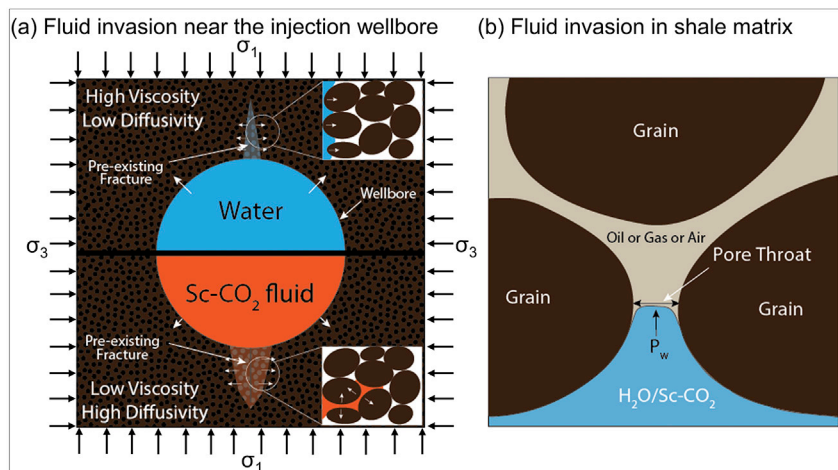
Fig. 14. (a) Fluid invasion near the injection wellbore. Due to the low viscosity and high diffusivity of Sc-CO_2 a large affected area is created near pre-existing natural fractures or flow channels. (b) In the area distant from the injection wellbore, capillary effects determine that Sc-CO_2 enters pore throats as small as 5.7 nm, while H_2O may only penetrate pore throats larger than 12.9 nm.
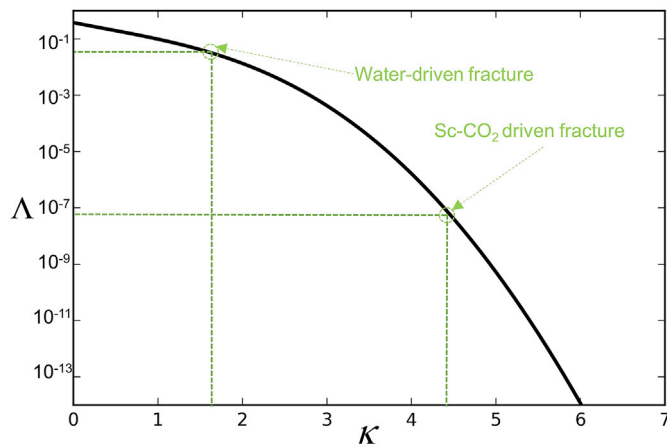
Fig. 15. The relationship between dimensionless lag length (Λ) and dimensionless toughness (κ) (Garagash and Detournay, 2000).

larger roughness and complexity; high viscosity fluid has a larger fluid lag at the fracture tip and creates a relatively smooth fracture surface. Here, we need to clarify that it may be a potential mechanism on controlling fracture surface roughness since one of limitations of our experiment is that the fluid lag phenomenon cannot be observed or measured in our experiments. Further research may be carried to investigate the fluid lag control on fracture surface roughness.

4.2. Fluid flow in a single fracture

Helium flow (q) in a single fracture after H_2O or Sc-CO_2 fracturing can be estimated by the cubic law as (Brown, 1987):

$$q = -\frac{e^3}{12\mu}\frac{\partial P}{\partial x}$$ (14)

where e [m] is fracture aperture.

With the effect of fracture roughness, the cubic law may be rewritten by considering a coefficient of correction (Witherspoon et al., 1980):

$$q = -\frac{e^3}{12\mu}\frac{\partial P}{\partial x}\cdot\frac{1}{1+6\left(\frac{\Delta}{\overline{e}}\right)^{1.5}}$$ (15)

where $\overline{e}$ [m] is the effective hydraulic fracture aperture; and Δ[m] is the arithmetic mean height (S_a), as measured by profilometry.

The permeability of samples both before and after fracturing can be evaluated from:

$$q = -\frac{k\cdot A}{\mu}\frac{\partial P}{\partial x}$$ (16)

where A [m^2] is cross-section area of sample

Table 3
The parameters and results for estimating fluid lag length.

Parameters	Values (H_2O)	Values (Sc-CO_2)	Units
Fluid viscosity/μ	900	150	μPa·s
Fracture propagation velocity/V	136.0		m/s
Young's Modulus/E	25.0		GPa
Poisson's ratio/ν	0.25		–
Far-field stress/σ_0	10		MPa
Fracture toughness/K_{IC}	1		MPa·m$^{1/2}$
Estimation Results			
Parameter/L_μ	0.007699	0.001283	m
Parameter/L_κ	0.025465	0.025465	m
Dimensionless toughness/κ	1.818641	4.454742	–
Dimensionless lag length/Λ	0.015488	2.04174×10^{-8}	–
Fluid lag length/λ	119.247	2.61996×10^{-5}	μm

Combining Eq. (15) to Eq. (16), the relationship between average aperture and permeability is described as:

$$\frac{\overline{e}^3}{12+72\left(\frac{\Delta}{\overline{e}}\right)^{1.5}} = k\cdot A$$ (17)

Based on Eq. (17), the effective hydraulic aperture $\overline{e}$ after Sc-CO_2 and H_2O fracturing is shown in Fig. 16.

The fracture aperture reduces with the increasing effective stress. The average aperture of the Sc-CO_2 and H_2O fractured fractures are 7.08 μm and 1.46 μm, respectively. The effective hydraulic fracture aperture to Sc-CO_2 fracturing, is ~4.85 times larger than that to H_2O fracturing, implying that Sc-CO_2 fracturing may potentially benefit shale gas recovery.

4.3. Permeability enhancement due to mineral grain removal

The induced fractures remain imperfectly mated after the fracturing and for the measurement of permeability. To investigate potential mechanisms for this self-propping, stylus profilometry is applied at a same location for the two sides of the imperfectly mated fracture.

Fig. 17 indicate that the slice profile height at the same location has a similar profile but cannot match perfectly for both Sc-CO_2 and H_2O fractured samples. A larger profile difference is observed for the Sc-CO_2 fracturing samples. For the H_2O fractured samples, the largest difference is 77.67 μm while for the Sc-CO_2 fractured samples, the largest difference reaches 196.30 μm. In addition, the sample is thoroughly cleaned with DI water before the stylus profilometry tests. We conjecture that the removal of grains acts micro proppants and result in greater apertures in the fractures. Thus during permeability measurements, those removed mineral grains remain in the fractures and act as micro proppants retain the fractures open even with applied confining stress.

This removal and presence of mineral grains by Sc-CO_2 fracturing has also been previously observed (but not discussed) (Ishida et al., 2016) as illustrated in Fig. 17 (c). This shows a petrographic image to compare fracture patterns between Sc-CO_2 fracturing and viscous oil fracturing. Fractures induced by Sc-CO_2 propagate mainly along the grain boundaries of the minerals while fractures induced by viscous oil cut through mineral grains and propagate almost directly along the direction of maximum principal stress.

We summarize two possible mechanisms that explain how mineral grains are removed and redistributed in the case of Sc-CO_2 fracturing. (1) Sc-CO_2 fracturing tends to be more energetic in developing fractures – this is in accordance with the macroscopic observation that Sc-CO_2 splits the sample into two halves while H_2O creates a narrow fracture (Fig. 5).
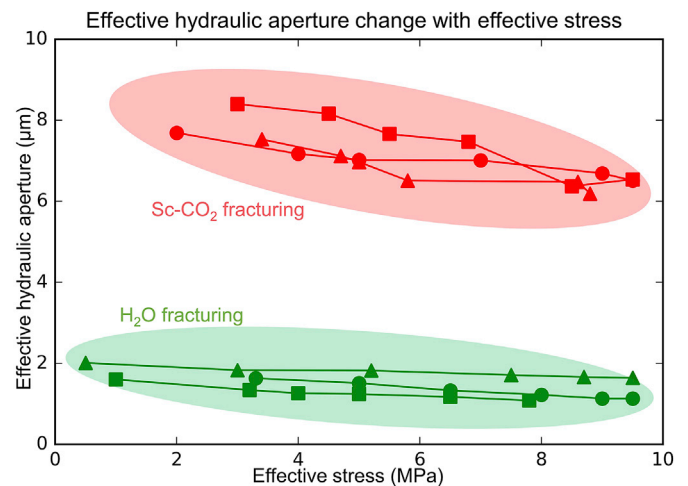
Fig. 16. Effective hydraulic aperture change with effective stress for Sc-CO_2 and H_2O fractured samples.
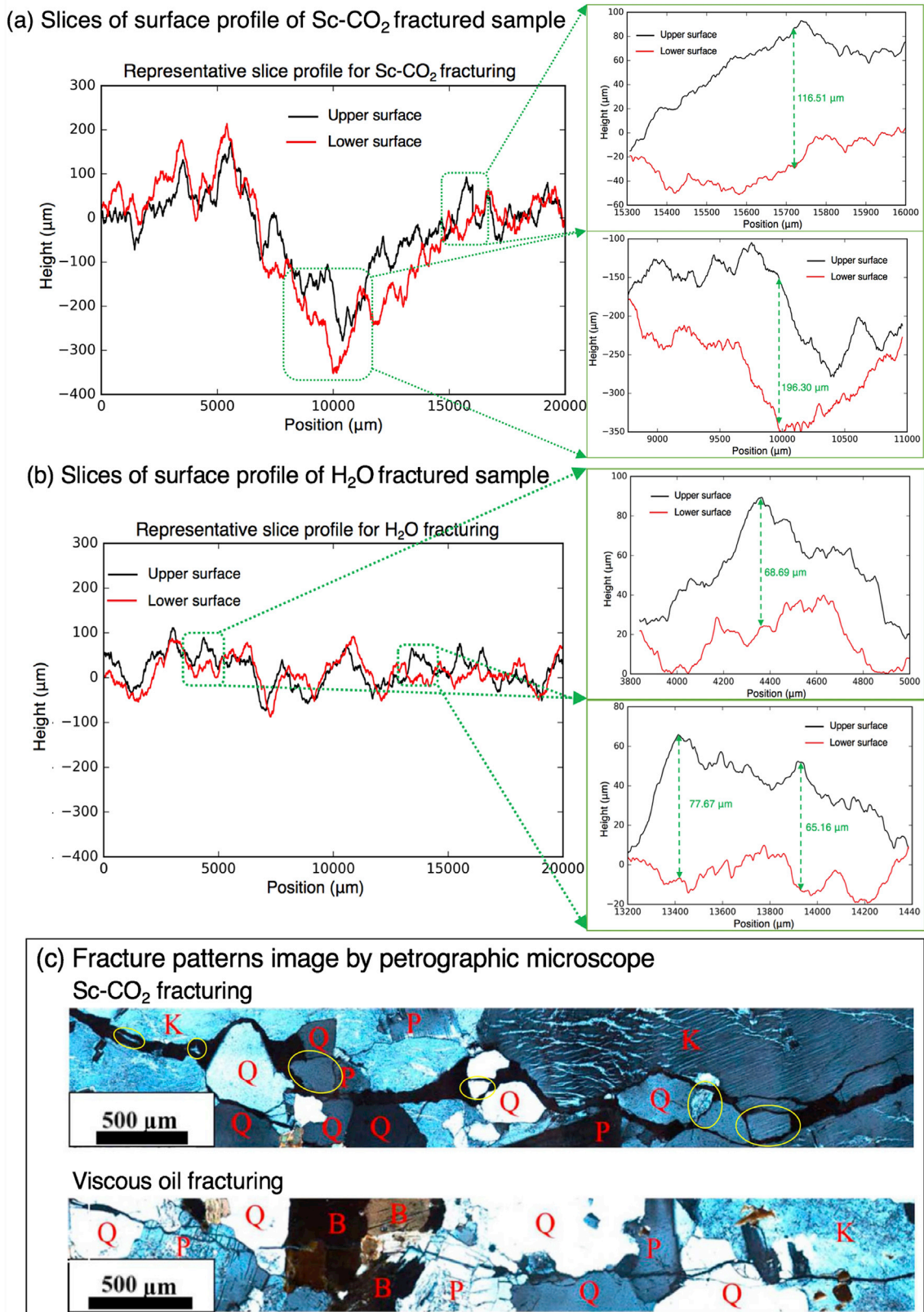
Fig. 17. (a) Surface profile of Sc-CO$_2$ fractured sample. The maximum profile difference is ~196 μm; (b) Surface profile of H$_2$O fractured sample. The maximum profile difference is ~78 μm. (c) Fracture patterns imaged by petrographic microscope. (B: biotite, K: K-feldspar, P: plagioclase, Q: quartz). (Modified from Ishida et al., 2016). The yellow circles are minerals grains that have been peeled from the fractue surface. (For interpretation of the references to colour in this figure legend, the reader is referred to the Web version of this article.)
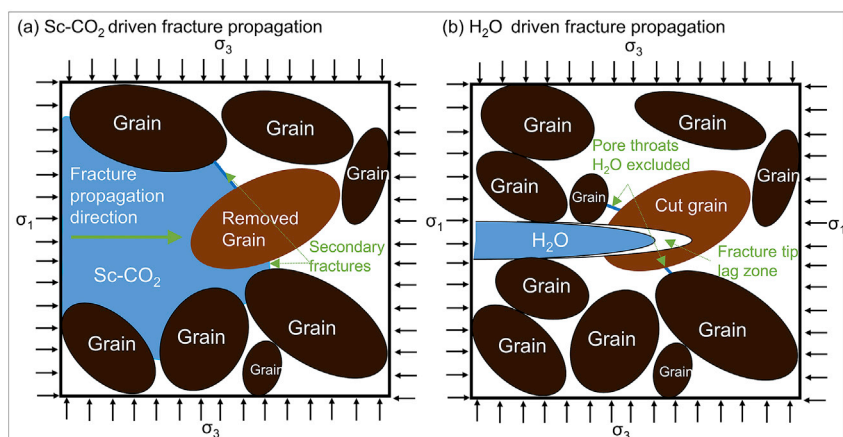
Fig. 18. (a) Sc-CO_2 driven fracture propagation; (b) H_2O driven fracture propagation. Sc-CO_2 can enter small pore throats that H_2O excludes. Mineral grains between two secondary minor fractures may be possibly removed from the fracture surface when fractured by Sc-CO_2.

(2) Mechanisms of propagation are different between Sc-CO_2 and H_2O driven fractures. In Fig. 18, Sc-CO_2 enters through much smaller pore throats than H_2O and creates more micro- and secondary fractures (Ishida et al., 2016; Zhang et al., 2016). Hence, in the fracture propagation process, Sc-CO_2 enters small pore throats and weakens the mineral cementation. As a result, mineral grains between two secondary or minor fractures are possibly peeled from the fracture surface. For H_2O fracturing, the fluid cannot enter those small pore throats and needs to cut through mineral grains to keep fracture propagating, as observed in Fig. 17 (c). In that case, the mineral grain is damaged but mineral cementation still bonds the grains. At same time, Fig. 18 also illustrates why larger fracture tortuosity is observed for Sc-CO_2 fracturing than H_2O fracturing which observed in Fig. 7. In the fracture tip, Sc-CO_2 can penetrate into pre-existing defects and grain boundaries more easily than H_2O. Hence, fractures propagate into the randomly oriented grain boundary, which results to a high fracture tortuosity.

In summary, the primary cause for the larger permeability enhancement by Sc-CO_2 fracturing over H_2O is that larger mineral grains are peeled from the fracture surface by Sc-CO_2 fracturing, which then acts as a micro proppant to retain the fracture open.

5. Conclusion

We have conducted hydraulic fracturing experiments to evaluate the difference between fracturing with Sc-CO_2 and H_2O and draw the following conclusions:

(1) Small-scale laboratory fracturing experiments indicate that Sc-CO_2 fracturing tends to be more energetic. Sc-CO_2 fracturing transects the shale sample into two halves while conventional H_2O fracturing only creates narrow fractures and an incomplete transection. In addition, Sc-CO_2 fracturing creates fractures with larger tortuosity relative to H_2O fracturing. Results suggest that Sc-CO_2 fracturing may induce greater damage to the shale and potentially result in improved performance over H_2O fracturing (in the laboratory). Ultimately this may create more fractures and result in better performance in the treatment of shale reservoirs.

(2) Sc-CO_2 fracturing can generate fracture surfaces with a larger roughness and complexity due to its low viscosity, high diffusivity and low interfacial tension. Mechanisms determine fracture surface roughness are discussed based on fluid diffusion, capillary effect and fluid lag phenomenon. Results suggest that Sc-CO_2 fracturing has the potential to create a larger exposed area to benefit fracturing treatment in shale formations.

(3) Given the same stress conditions, Sc-CO_2 fracturing has increased the permeability of shale by five orders of magnitude - about three orders of magnitude greater than hydraulic fracturing (absent proppant). This is supported by the observation that mineral grains are peeled from the induced fracture surface by Sc-CO_2 fracturing and act as micro proppants that retain a larger fracture aperture when the fracture deflates after fracturing. This suggest that Sc-CO_2 fracturing has a better fracturing performance than water in enhancing shale permeability during shale reservoir treatment.

These experimental results validate the potential of Sc-CO_2 as a fracturing fluid in shale gas stimulation due to its better performance in creating rougher fracture surface and permeability enhancement However, successful application of Sc-CO_2 as a fracturing fluid requires good performance on fluid leak-off, fluid discharge, sand-carrying ability which will be further studied. However, successful application of Sc-CO_2 as a fracturing fluid requires good performance on fluid leak-off, fluid discharge, sand-carrying ability which will be further studied. In addition, expense increase cannot be neglected since the successful impletion of Sc-CO_2 fracturing operations require a series fundamental works such as CO_2 capture, storage, delivery, pressurizing and treatment of flow-back CO_2.

Nomenclature

S_a	The arithmetic mean roughness, μm
S_q	The root meansquare(RMS) roughness, μm
S_z	The maximum height of the surface, μm

D	Fractal dimension, dimensionless
μ	Fluid viscosity, Pa·s
β	Fluid compressibility, Pa^{-1}
k	Permeability, m^2
C	Frature tortuosity,dimensionless
x	Diffusion length, m
D_d	Diffusion coefficient, m^2/s
t	Diffusion time, s
P_c^*	Entry pressure for fluid to enter the pore throat, Pa
σ	Interfacial tension, N/m
θ	Contact angle, °
d^*	Critical pore throat size, m
L_μ	Parameter associated with viscous dissipation, m
V	Fracture and fluid propagation velocity, m/s
E'	Plane-strain modulus, MPa
E	Young's modulus, GPa
ν	Poisson ratio, dimensionless
σ_0	Far-field stress, MPa
K_{IC}	Fracture toughness, MPa·m$^{1/2}$
L_μ	A parameter associated with viscous dissipation, m
L_κ	A parameter that characterizes the dissipation due to fracturing of the solid, m
κ	Dimensionless toughness, dimensionless
Λ	Dimensionless fluid lag length, dimensionless
λ	Fluid lag length, m
q	Flow rate, m^3/s
e	Fracture aperture, m
$\bar{e}$	Effective hydraulic fracture aperture, m
Δ	Surface arithmetic mean height, m

References

Arakawa, K., Takahashi, K., 1991. Relationships between fracture parameters and fracture surface roughness of brittle polymers. Int. J. Fract. 48 (2), 103–114. https://doi.org/10.1007/BF00018393.

Arthur, D.J., Bohm, B., Coughlin, B.J., Layne, M., 2008. Hydraulic fracturing considerations for natural gas wells of the fayetteville shale. Consultant (Phila.) 1–19. Link. http://www.aogc2.state.ar.us/OnlineData/reports/ALL%20FayettevilleFrac%20FINAL.pdf.

Brace, W.F., Walsh, J.B., Frangos, W.T., 1968. Permeability of granite under high pressure. J. Geophys. Res. 73 (6), 2225–2236. https://doi.org/10.1029/JB073i006p02225.

Brown, S.R., 1987. Fluid flow through rock joints: the effect of surface roughness. J. Geophys. Res. 92 (B2), 1337–1347. https://doi.org/10.1029/JB092iB02p01337.

Candela, T., Renard, F., Bouchon, M., Brouste, A., Marsan, D., Schmittbuhl, J., Voisin, C., 2009. Characterization of fault roughness at various scales: implications of three-dimensional high resolution topography measurements. Pure Appl. Geophys. 166 (10–11), 1817–1851. https://doi.org/10.1007/s00024-009-0521-2.

Chen, Y., Nagaya, Y., Ishida, T., 2015. Observations of fractures induced by hydraulic fracturing in anisotropic granite. Rock Mech. Rock Eng. 48 (4), 1455–1461. https://doi.org/10.1007/s00603-015-0727-9.

Ciriello, V., Longo, S., Chiapponi, L., Di Federico, V., 2016. Porous gravity currents: a survey to determine the joint influence of fluid rheology and variations of medium properties. Adv. Water Resour. 92, 105–115. https://doi.org/10.1016/j.advwatres.2016.03.021.

Clarkson, C.R., 2013. Production data analysis of unconventional gas wells: Workflow. Int. J. Coal Geol. 109–110, 147–157. https://doi.org/10.1016/j.coal.2012.11.016.

Dahaghi, A.K., 2010. Numerical simulation and modeling of enhanced gas recovery and CO$_2$ sequestration in shale gas reservoirs: a feasibility study. SPE Int. Conf. CO2 Capture, Storage, Util. https://doi.org/10.2118/139701-MS.

Desroches, J., Detournay, E., Lenoach, B., Papanastasiou, P., Pearson, J.R.A., Thiercelin, M., Cheng, A., 1994. The crack tip region in hydraulic fracturing. In Proceedings of the Royal Society of London A: Mathematical. Physical and Engineering Sciences 447, 39–48. https://doi.org/10.1098/rspa.1994.0127.

Detournay, E., 2004. Propagation regimes of fluid-driven fractures in impermeable rocks. Int. J. GeoMech. 4, 35–45. https://doi.org/10.1061/(ASCE)1532-3641(2004)4:1(35).

Detournay, E., 2016. Mechanics of hydraulic fractures. Annu. Rev. Fluid Mech. 48, 311–339. https://doi.org/10.1146/annurev-fluid-010814-014736.

Detournay, E., Carbonell, R., 1997. Fracture-mechanics analysis of the breakdown process in minifracture or leakoff test. SPE Prod. Facil. 12, 29–31. https://doi.org/10.2118/28076-PA.

Espinoza, D.N., Santamarina, J.C., 2010. Water-CO2-mineral systems: interfacial tension, contact angle, and diffusion implications to CO2 geological storage. Water Resour. Res. 46, 1–10. https://doi.org/10.1029/2009WR008634.

Fang, Y., Elsworth, D., Wang, C., Ishibashi, T., Fitts, J.P., 2017. Frictional stability-permeability relationships for fractures in shales. J. Geophys. Res. Solid Earth 122, 1760–1776. https://doi.org/10.1002/2016JB013435.

Federico, V., Di, Longo, S., King, S.E., Chiapponi, L., Petrolo, D., Ciriello, V., 2017. Gravity-driven flow of Herschel – bulkley fluid in a fracture and in a 2D porous medium. J. Fluid Mech. 821, 59–84. https://doi.org/10.1017/jfm.2017.234.

Fenghour, A., Wakeham, W.A., Vesovic, V., 1998. The viscosity of carbon dioxide. J. Phys. Chem. Ref. Data 27, 31–44. https://doi.org/10.1063/1.556013.

Fernø, M.A., Hauge, L.P., Uno Rognmo, A., Gauteplass, J., Graue, A., 2015. Flow visualization of CO$_2$ in tight shale formations at reservoir conditions. Geophys. Res. Lett. 42, 7414–7419. https://doi.org/10.1002/2015GL065100.

Gadelmawla, E.S., Koura, M.M., Maksoud, T.M.A., Elewa, I.M., Soliman, H.H., 2002. Roughness parameters. J. Mater. Process. Technol. 123, 133–145. https://doi.org/10.1016/S0924-0136(02)00060-2.

Garagash, D.I., Detournay, E., 2000. The tip region of a fluid-driven fracture in an elastic medium. Trans. Soc. Mech. Eng. J. Appl. Mech 67 (1), 183–192. https://doi.org/10.1115/1.321162.

Hossain, M.M., Rahman, M.K., Rahman, S.S., 2000. Hydraulic fracture initiation and propagation: roles of wellbore trajectory, perforation and stress regimes. J. Petrol. Sci. Eng. 27, 129–149. https://doi.org/10.1016/S0920-4105(00)00056-5.

Hubbert, M.K., Willis, D.G., 1957. Mechanics of hydraulic fracturing. Trans. Am. Inst. Min. Eng 210, 53–168.

Ishida, T., Aoyagi, K., Niwa, T., Chen, Y., Murata, S., Chen, Q., Nakayama, Y., 2012. Acoustic emission monitoring of hydraulic fracturing laboratory experiment with supercritical and liquid CO$_2$. Geophys. Res. Lett. 39. https://doi.org/10.1029/2012GL052788.

Ishida, T., Chen, Y., Bennour, Z., Yamashita, H., Inui, S., Nagaya, Y., Naoi, M., Chen, Q., Nakayama, Y., Nagano, Y., 2016. Features of CO2 fracturing deduced from acoustic emission and microscopy in laboratory experiments. J. Geophys. Res.: Solid Earth. https://doi.org/10.1002/2016JB013365.

Jia, Y., Lu, Y., Elsworth, D., Fang, Y., Wang, C., Tang, J., 2017. Hydro-mechanical-chemical effects on permeability evolution of fractures in Longmaxi shale. In: Proceedings of the 51th US Rock Mechanics/Geomechanics Symposium (San Francisco, CA, USA).

Kestin, J., Sengers, J.V., Kamgar-Parsi, B., Sengers, 1984. Thermophysical properties of fluid H$_2$O. J. Phys. Chem. Ref. Data 13, 175–183. https://doi.org/10.1063/1.555707.

Leach, R., 2013. Characterization of Areal Surface Texture, Berlin. https://doi.org/10.1007/978-3-642-36458-7.

Li, X., Feng, Z., Han, G., Elsworth, D., Marone, C., Saffer, D., Cheon, D.-S., 2016. Breakdown pressure and fracture surface morphology of hydraulic fracturing in shale with H$_2$O, CO$_2$ and N$_2$. Geomech. Geophys. Geo-Energy Geo-Resources 2, 63–76. https://doi.org/10.1007/s40948-016-0022-6.

Longo, S., Di Federico, V., 2015. Unsteady flow of shear-thinning fluids in porous media with pressure-dependent properties. Transport Porous Media 110, 429–447. https://doi.org/10.1007/s11242-015-0565-y.

Longo, S., Ciriello, V., Chiapponi, L., Di Federico, V., 2015. Combined effect of rheology and confining boundaries on spreading of gravity currents in porous media. Adv. Water Resour. 79, 140–152. https://doi.org/10.1016/j.advwatres.2015.02.016.

Lu, Y., Ao, X., Tang, J., Jia, Y., Zhang, X., Chen, Y., 2016. Swelling of shale in supercritical carbon dioxide. J. Nat. Gas Sci. Eng. 30, 268–275. https://doi.org/10.1016/j.jngse.2016.02.011.

Mandelbrot, Benoit B., Pignoni, Roberto, 1983. The Fractal Geometry of Nature, vol. 173. WH freeman, New York.

McClure, M.W., 2014. Stimulation mechanism and the direction of propagation of microseismicity. Thirty-Ninth Work Geotherm. Reserv. Eng. Stanford University 1–16.

Middleton, R.S., Carey, J.W., Currier, R.P., Hyman, J.D., Kang, Q., Karra, S., Jiménez-Martínez, J., Porter, M.L., Viswanathan, H.S., 2015. Shale gas and non-aqueous fracturing fluids: opportunities and challenges for supercritical CO_2. Appl. Energy 147, 500–509. https://doi.org/10.1016/j.apenergy.2015.03.023.

Miller, C., Waters, G., Rylander, E., 2011. Evaluation of production log data from horizontal wells drilled in organic shales. North Am. Unconv. Gas Conf. Exhib. https://doi.org/10.2118/144326-ms. SPE 144326.

Myers, T., 2012. Potential contaminant pathways from hydraulically fractured shale to aquifers. Ground Water 50, 872–882. https://doi.org/10.1111/j.1745-6584.2012.00933.x.

Odumabo, S.M., Karpyn, Z.T., Ayala, H.L.F., 2014. Investigation of gas flow hindrance due to fracturing fluid leakoff in low permeability sandstones. J. Nat. Gas Sci. Eng. 17, 1–12. https://doi.org/10.1016/j.jngse.2013.12.002.

Osborn, S.G., Vengosh, A., Warner, N.R., Jackson, R.B., 2011. Methane contamination of drinking water accompanying gas-well drilling and hydraulic fracturing. Proc. Natl. Acad. Sci. Unit. States Am. 108, 8172–8176. https://doi.org/10.1073/pnas.1100682108.

Palmer, I.D., Moschovidis, Z.A., Cameron, J.R., others, 2007. Modeling shear failure and stimulation of the Barnett Shale after hydraulic fracturing. SPE Hydraul. Fract. Technol. Conf. https://doi.org/10.2118/106113-MS.

Pei, P., Ling, K., He, J., Liu, Z., 2015. Shale gas reservoir treatment by a CO_2-based technology. J. Nat. Gas Sci. Eng. 26, 1595–1606. https://doi.org/10.1016/j.jngse.2015.03.026.

Pentland, A.P., 1984. Fractal-based description of natural scenes. IEEE Trans. Pattern Anal. Mach. Intell. 661–674. https://doi.org/10.1109/TPAMI.1984.4767591. PAMI-6.

Philibert, J., 2006. One and a half century of diffusion: fick, Einstein, before and beyond. Diffus. Fundam 4 (6), 1–19.

Renard, F., Voisin, C., Marsan, D., Schmittbuhl, J., 2006. High resolution 3D laser scanner measurements of a strike-slip fault quantify its morphological anisotropy at all scales. Geophys. Res. Lett. 33, 33–36. https://doi.org/10.1029/2005GL025038.

Renshaw, C.E., Harvey, C.F., 1994. Propagation velocity of a natural hydraulic fracture in a poroelastic medium. J. Geophys. Res. 99, 21667–21677. https://doi.org/10.1029/94JB01255.

Scanlon, B.R., Reedy, R.C., Nicot, J.P., 2014. Comparison of water use for hydraulic fracturing for unconventional oil and gas versus conventional oil. Environ. Sci. Technol. 48, 12386–12393. https://doi.org/10.1021/es502506v.

Shapiro, S.A., Dinske, C., 2009. Fluid-induced seismicity: pressure diffusion and hydraulic fracturing. Geophys. Prospect. 57, 301–310. https://doi.org/10.1111/j.1365-2478.2008.00770.x.

Vengosh, A., Warner, N., Jackson, R., Darrah, T., 2013. The effects of shale gas exploration and hydraulic fracturing on the quality of water resources in the United States. Procedia Earth Planet. Sci. 7, 863–866. https://doi.org/10.1016/j.proeps.2013.03.213.

Vengosh, A., Jackson, R.B., Warner, N., Darrah, T.H., Kondash, A., 2014. A critical review of the risks to water resources from unconventional shale gas development and hydraulic fracturing in the United States. Environ. Sci. Technol. 48, 8334–8348. https://doi.org/10.1021/es405118y.

Wang, Y., Liu, S., Elsworth, D., 2015. Laboratory investigations of gas flow behaviors in tight anthracite and evaluation of different pulse-decay methods on permeability estimation. Int. J. Coal Geol. 149, 118–128. https://doi.org/10.1016/j.coal.2015.07.009.

Wang, S., Javadpour, F., Feng, Q., 2016. Confinement correction to mercury intrusion capillary pressure of shale nanopores. Sci. Rep. 6, 20160. https://doi.org/10.1038/srep20160.

Wang, Z., Sun, B., Sun, X., 2016. Calculation of temperature in fracture for carbon dioxide fracturing. SPE J. 21 (05), 1491–1500. https://doi.org/10.2118/180930-PA.

Wang, C., Elsworth, D., Fang, Y., 2017. Influence of weakening minerals on ensemble strength and slip stability of faults. J. Geophys. Res. Solid Earth 122, 7090–7110. https://doi.org/10.1002/2016JB013687.

Wang, J., Elsworth, D., Wu, Y., Liu, J., Zhu, W., Liu, Y., 2017. The influence of fracturing fluids on fracturing processes: a comparison between water, oil and SC-CO_2. Rock Mech. Rock Eng. 299–313. https://doi.org/10.1007/s00603-017-1326-8.

Warpinski, Norman R., Du, Jing, Zimmer, Ulrich, 2012. Measurements of hydraulic-fracture-induced seismicity in gas shales. In: SPE Hydraul. Fract. Technol. Conf. Woodlands,Texas,USA.

Witherspoon, P.A., Wang, J.S.Y., Iwai, K., Gale, J.E., 1980. Validity of Cubic Law for fluid flow in a deformable rock fracture. Water Resour. Res. 16, 1016–1024.

Yuan, B., Su, Y., Moghanloo, R.G., Rui, Z., Wang, W., Shang, Y., 2015a. A new analytical multi-linear solution for gas flow toward fractured horizontal wells with different fracture intensity. J. Nat. Gas Sci. Eng. 23, 227–238. https://doi.org/10.1016/j.jngse.2015.01.045.

Yuan, B., Wood, D.A., Yu, W., 2015b. Stimulation and hydraulic fracturing technology in natural gas reservoirs: theory and case studies (2012-2015). J. Nat. Gas Sci. Eng. 26, 1414–1421. https://doi.org/10.1016/j.jngse.2015.09.001.

Yuan, B., Ghanbarnezhad Moghanloo, R., Shariff, E., 2016. Integrated investigation of dynamic drainage volume and inflow performance relationship (transient IPR) to optimize multistage fractured horizontal wells in tight/shale formations. J. Energy Resour. Technol. 138, 52901. https://doi.org/10.1115/1.4032237.

Yuan, B., Zheng, D., Moghanloo, R.G., Wang, K., 2017. A novel integrated workflow for evaluation, optimization, and production predication in shale plays. Int. J. Coal Geol. 180, 18–28. https://doi.org/10.1016/j.coal.2017.04.014.

Zhang, X., Lu, Y., Tang, J., Zhou, Z., Liao, Y., 2016. Experimental study on fracture initiation and propagation in shale using supercritical carbon dioxide fracturing. Fuel 190, 370–378. https://doi.org/10.1016/j.fuel.2016.10.120.